ACS APPLIED MATERIALS & INTERFACES

Research Article

www.acsami.org

Engineering of Monodisperse Mesoporous Titania Beads for Photocatalytic Applications

Xingdong Wang,[†] Lu Cao,[§] Dehong Chen,[§] and Rachel A. Caruso*[,†,§]

[†]CSIRO Materials Science and Engineering, Clayton, Victoria 3168, Australia

[§]PFPC, School of Chemistry, The University of Melbourne, Melbourne, Victoria 3010, Australia

Supporting Information

ABSTRACT: The properties of monodisperse mesoporous TiO_2 beads were readily tuned by varying the temperature (500−800 °C) and time (2−24 h) of calcination for solvothermally treated hexadecylamine/TiO_2 hybrid assemblies. The crystal properties (crystal phase, crystallite size, and crystallinity), surface and pore properties (surface hydroxyl groups, surface area, porosity, and pore size), and diameter of the beads were significantly altered with these changes in calcination conditions. These properties played an important role in determining the photocatalytic activity of the materials, which was assessed by monitoring the photodegradation of a methylene blue solution under ultraviolet light. The maximum activity was achieved with the materials that were calcined at 650 °C for 2−8 h with a bead diameter around 700 nm. High activity was attributed to the balance of high crystallinty of the anatase phase, high porosity and large surface area. The size of the beads made separation easy for the reuse of the material after reaction. The synthesis−properties−photocatalytic activity relationships of these monodisperse mesoporous TiO_2 beads have been established.

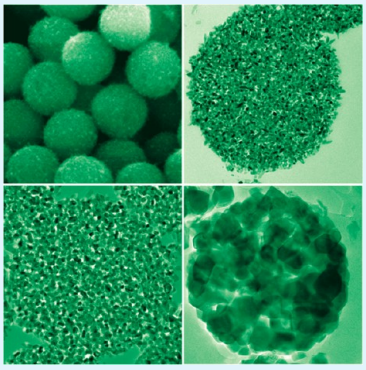

KEYWORDS: *titanium dioxide, nanostructure, mesoporous, beads, photocatalysts*

1. INTRODUCTION

The requirement for materials to combat environmental pollution and proposed future energy demands has attracted attention in both research and industrial settings.[1−6] TiO_2-based materials have been of interest for such purposes due to their unique electronic and optical properties, which yield applications in the photocatalytic degradation of organic pollutants,[3] photolysis of water to yield H_2 fuel,[4] photovoltaics and energy storage.[7] Other advantages of TiO_2 materials, such as excellent chemical stability, abundance, low cost, and low toxicity, ensure significant research attention.[1,3]

In terms of environmental pollution remediation, the intrinsic issues of TiO_2 materials have limited its activity and therefore hampered its practical application as a photocatalyst.[1,3] For example, (i) the high recombination of photoexcited electron and hole pairs leads to low quantum yield; (ii) low light harvesting due to the wide band gap of the material (3.2 eV for anatase TiO_2 materials) that only allows ultraviolet light (less than 5% of solar energy reaching the earth's surface) to induce the reaction; and (iii) problems relating to recycling of the high surface area photocatalysts that are generally nanoparticles.[1,3,8] Therefore, materials development to overcome these difficulties are crucial. Significant effort has focused on compositional control by adding foreign elements to alter the TiO_2 properties. For example, (i) decreasing the recombination of photon induced electron−hole pairs by using noble metal nanoparticle deposition (Au, Pd, Ag, or Pt), where the nanoparticles serve as electron sinks separating the excited electron from the hole;[9,10] (ii) doping of elements into the TiO_2 crystal lattice to decrease the band gap thereby allowing light absorption in the visible range;[11,12] and (iii) incorporating magnetic particles to assist with the separation of the photocatalyst;[13,14] however, this generally requires an external magnetic field, which is inconvenient and costly.

In recent years, morphological control,[15,16] through variation of material dimension or porosity, is emerging as a promising solution to deal with the above issues. This has resulted in a range of structures including grid-like,[17] nanocolumn arrays,[18] monolithic,[19,20] fibers,[21] nanorods,[22] flower-like structures,[23] nanosheets,[24] spheres,[25,26] and their hollow structures.[27−29] Among these morphologies, mesoporous spheres, which are aggregates of nanosized TiO_2 crystallites, have aroused wide research interest, prepared using either template[26] or template free methods.[30] Specifically, submicrometer sized mesoporous beads have attracted much attention for photocatalytic application due to their improved light absorbance and ease of separation for reuse.[31,32] However, the synthesis of these submicrometer TiO_2 spheres was either complicated, required specific facilities (aerosol-spray assisted setup),[31,32] or produced nonuniform spheres.[30−32] Recently, monodisperse mesoporous beads with controlled bead diameters (300−800 nm) and pore sizes (14−23 nm) have been produced by a facile method that couples sol−gel chemistry and solvothermal techniques (using

Received: May 17, 2013
Accepted: September 3, 2013
Published: September 23, 2013

hexadecylamine as a structure-directing agent), and have demonstrated high efficiencies in dye-sensitized solar cells.[33−36] The uniform size distribution and submicrometer diameter, and also the convenient preparation method make them a potential candidate to address the above-mentioned issues of TiO_2 materials in photocatalysis.

The photocatalytic activity of TiO_2 is significantly influenced by the crystal phase, crystallinity, surface area, and porosity.[3,37] High crystallinity produces less surface defects, which benefits the charge transfer and therefore decreases the recombination of excited electron and hole pairs.[3,37,38] For photocatalysis, generally anatase is the preferable phase. To increase the crystallinity, high temperature calcination is required. However, at temperatures over 600 °C, this will lead to phase conversion from anatase to the less photocatalytic active rutile, decreased surface area, and easy pore collapse.[3,37,39,40]

In our previous studies,[33−36] the parameters during the sol−gel synthesis and solvothermal treatment were varied to successfully control the bead diameter, morphology, monodispersity, surface area and pore size for improving the effectiveness of these materials as electrodes in the dye-sensitized solar cell. Other physical and chemical properties such as the crystal size, thermal stability of the crystal phase, crystallinity and surface chemistry were more important here for the development of efficient photocatalysts. Therefore, the properties of the beads have been tuned for photocatalytic application by varying the calcination temperature (from 500 to 800 °C) and time (from 2 to 24 h). The anatase phase was retained and the crystallinity increased significantly after high temperature treatment (up to 800 °C). The effect of calcination temperature and time on the bead properties including crystal properties, surface properties and porosity was systematically analyzed, and the photocatalytic activity, which was assessed by photodecomposition of methylene blue under UV light, was determined. The correlation between calcination conditions, materials properties, and photocatalytic activities was therefore established. The mesoporosity within the beads and large internal surface areas benefit the diffusion of the organic pollutant and accessibility to the active centers on the surfaces throughout the TiO_2 materials. High crystallinity of the anatase phase decreases the recombination of excited electron and hole pairs as there is a higher charge transfer capacity due to less surface defects. The submicrometer size of the beads improves the recyclability of the materials after the photocatalytic reaction as they can be removed either by simple sedimentation or by combining with membrane technology, therefore avoiding fouling associated with the use of nanoparticulate photocatalysts.

2. EXPERIMENTAL SECTION

2.1. Materials. Hexadecylamine (HDA, 90%, Sigma−Aldrich), absolute ethanol (>99.5% Chem-Supply), titanium (IV) isopropoxide (TIP, 97%, Sigma−Aldrich), potassium chloride (AR, BDH), ammonia solution (25%, Merck), methylene blue (MB, BDH Chemical Ltd.) and deionized water (18.2 MΩ cm) were used as received without further purification.

2.2. Synthesis of TiO_2 Beads. Hybrid amorphous mesostructured HDA/TiO_2 precursor beads were prepared according to the previously reported method.[36] Briefly, 7.95 g of HDA was dissolved in 800 mL absolute ethanol and aqueous potassium chloride (3.2 mL, 0.1 M) was added. TIP (18.1 mL) was then added at once under vigorous stirring. The resulting suspension sat for 16 h before the precursor beads were collected by centrifugation and washed with absolute ethanol three times. After drying at room temperature, 1.6 g of amorphous precursor beads was solvothermally treated at 160 °C for 16 h in a mixture of 20 mL ethanol and 10 mL Milli-Q water, with an ammonia concentration of 0.45 M. To remove the HDA template and tune the bead properties for photocatalytic application, the solvothermally treated beads were calcined at temperatures from 500 to 800 °C at 50 °C intervals for 2, 4, 8, 12, or 24 h in flowing air.

2.3. Characterization of TiO_2 Beads. A field emission environmental scanning electron microscope (Quanta 200F FEI) was used to examine the morphologies of the samples. All the images were obtained under low vacuum mode without sputter coating. For Transmission Electron Microscopy (TEM) analysis, the samples were embedded in an LR-white resin and ultramicrotomed into sections with a thickness of ∼90 nm. TEM examination was carried out using a FEI Tecnai F20 microscope operating at 200 kV. X-Ray powder diffraction (Australian Synchrotron powder diffractometer beamline with a beam energy of 15 kV) was used to verify crystal phase and estimate the crystal sizes of the resulting mesoporous TiO_2 beads. Nitrogen gas sorption isotherms were obtained at −196 °C using a Micromeritics Tristar 3000 surface area and porosity analyzer. All the samples were degassed at 160 °C overnight on a vacuum line prior to measurement. The standard multipoint Brunauer−Emmett−Teller (BET) method was utilized to calculate the specific surface area. The pore size distribution of the materials was derived from the adsorption branch of the isotherms based on the Barrett−Joyner−Halenda (BJH) model. The porosity of the material (P_m) was calculated by the equation of $P_m = V_p/(d^{-1} + V_p)$, where V_p and d refer to the pore volume and density of anatase (3.895 g cm^{-3}), respectively.[41] FT-IR was conducted on a PerkinElmer Spectrometer 400 FT-IR (Mid/NIR) with the Spectrum Software V6, equipped with a universal attenuated total reflectance (ATR) accessory. The powdered sample was placed onto an ATR diamond crystal and the spectrum with 4 scans at 4 cm^{-1} resolution was collected. The background spectrum was checked between each run.

2.4. Photocatalytic Activity Measurement. An Oriel 500 W Hg (Xe) globe from a 450−1000 W Oriel research arc lamp system was used to provide light of wavelength 200−2500 nm. An aluminum liquid filter (Oriel, DI water only) was used to remove unwanted IR heat. A band gap filter UG5 (Schott Company) was also attached to the liquid filter to transmit UV light (200−380 nm) to the reaction chamber. A 250 mL photocatalysis reaction chamber, jacketed with a distilled water circulation system to maintain a stable temperature of 20 ± 1 °C, was used. A thermometer was placed into the reaction solution to monitor the in situ temperature. Air (industrial grade) was bubbled continuously into the bottom of the reaction chamber to aerate the reaction system. The air flow rate was adjusted to 5 mL min^{-1} using a homemade control valve and titration tube with a soap meter. The photocatalytic reactions were started after the dye had reached adsorption−desorption equilibrium on the photocatalyst by mixing the photocatalyst (0.5 g L^{-1}) with the MB solution (50 mg L^{-1}, 160 mL) in the dark with stirring overnight. During the photocatalytic reaction, the UV−vis absorbance of the MB solution was monitored every 15 min to determine concentration changes.

3. RESULTS AND DISCUSSION

3.1. Materials Preparation. To obtain uniform submicrometer sized mesoporous TiO_2 beads, the HDA/TiO_2 hybrid beads were prepared by a sol−gel process where HDA acted as a structure directing agent and titanium(IV) isoproxide was the Ti source, followed by a solvothermal treatment in ethanol/water/ammonia mixtures at 160 °C for 16 h. [36] To address the shortcoming of photocatalyst separation and the ability to reuse the photocatalyst after photocatalytic reaction, a large diameter (∼800 nm) hybrid bead was chosen for this study. To tune the properties of these beads to obtain a high photocatalytic activity, as well as remove the HDA, the hybrid beads were calcined at various temperatures from 500 to 800 °C and times from 2 to 24 h. The calcination process affects the materials

properties and photocatalytic activity as detailed in the following sections.

3.2. Morphology and Diameter of the Beads. The beads were monodisperse in diameter regardless of the calcination conditions (Figure 1). Increasing the calcination

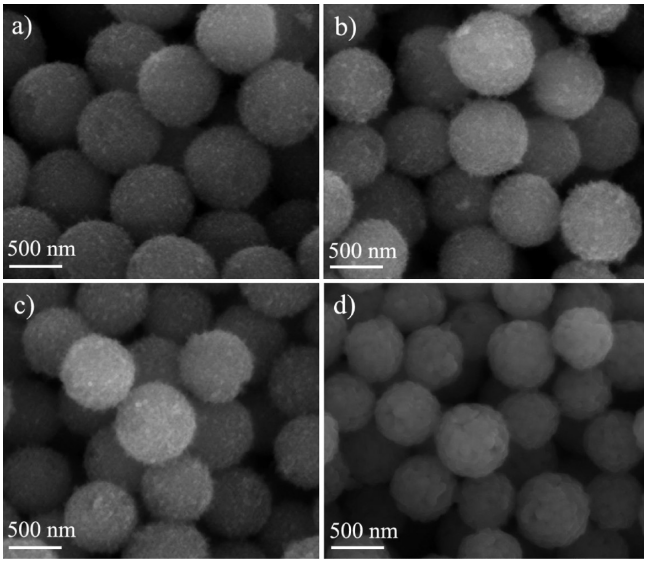

Figure 1. SEM images of the mesoporous TiO_2 beads calcined at (a) 500, (b and c) 650, and (d) 800 °C for 2 h, except panel c, which shows those calcined for 8 h.

temperature or time generally led to a decrease in the bead diameter with calcination temperature having a more significant effect on this shrinkage. Taking the materials calcined for 2 h as an example, the bead diameter decreased from 770 ± 20 to 700 ± 15 and to 460 ± 10 nm when the calcination temperature increased from 500 to 650 and to 800 °C, respectively (Figure 1 a, b and d). Increasing the calcination time from 2 to 8 h at 650 °C, the bead diameter slightly decreased from 700 ± 15 to 680 ± 20 nm (Figure 1 b and c). Shrinkage during clacination to remove the template has been commonly observed.[9,10]

3.3. Crystal Properties of the Beads. The crystal phase of the titania materials is crucial to photocatalytic activity. It is generally believed that the anatase phase gives higher photocatalytic activity than rutile and brookite.[42] As shown in Supporting Information Figure S2, the anatase phase was formed exclusively after solvothermal treatment. A further calcination treatment at 500 °C retained the anatase phase and enhanced the intensity of the anatase peaks. To monitor subtle changes in terms of the crystal growth or possible phase transition with increasing calcination temperature or time, high intensity and high resolution synchrotron X-ray powder diffraction was utilized. The anatase phase was obtained for the range of calcination temperatures (from 500 to 800 °C) and times (from 2 to 24 h at 650 °C) studied (Figure 2). No phase transition occurred even when the calcination temperature reached 800 °C, where transition from anatase to rutile phase would be expected.[40] The reason for the thermal stability of the anatase phase within the beads is currently under investigation and is beyond the scope of this manuscript. To obtain detailed crystal growth information, the intensity of each peak was tracked: The intensity increased with increase in either the calcination temperature or time, with temperature giving the greater enhancement.

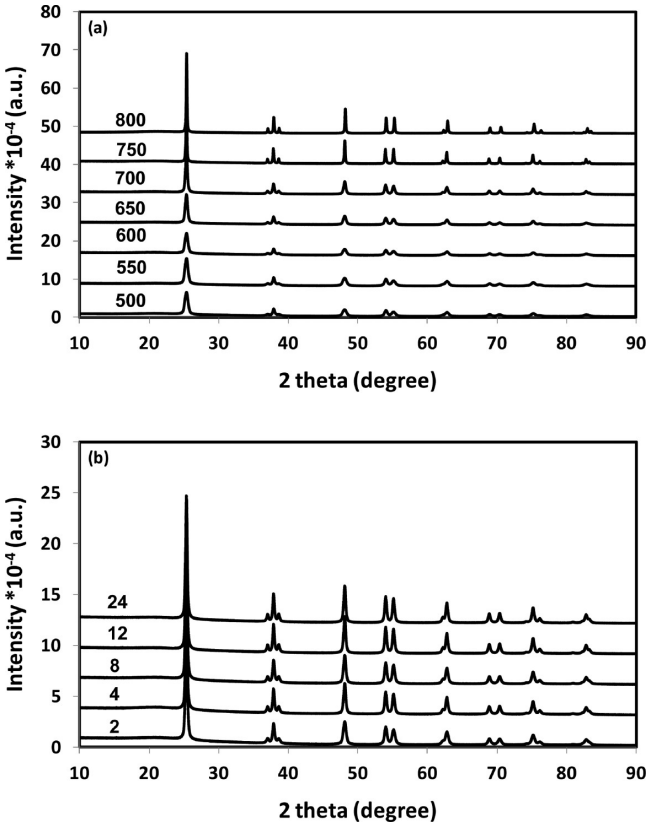

Figure 2. XRD patterns of the mesoporous TiO_2 beads calcined at different (a) temperatures from 500 to 800 °C for 2 h (subsequent patterns offset by 80 000) or (b) times from 2 to 24 h at 650 °C (subsequent patterns offset by 30 000).

The crystal size (calculated using the Scherrer equation at 2θ = 25.26°, Table 1) increased from 12.7 to 17.5 nm when the calcination temperature increased from 500 to 650 °C (2 h duration), then increased sharply from 17.5 to 55.0 nm when the calcination temperature increased from 650 to 800 °C (2 h duration). At a calcination temperature of 650 °C, the crystal size gradually grew from 17.5 to 25.8 nm when the calcination time increased from 2 to 24 h. The high crystallinity of anatase is crucial to promote the photocatalytic activity, as high crystallinity assists the charge transfer of the excited electron and hole pair, therefore decreasing the recombination.[43] A relative crystallinity[44] of the anatase beads was determined from the average ratio of each anatase peak intensity to that of the beads calcined at 800 °C for 2 h with highest crystallinity (used as a reference), where the relative crystallinity is denoted as 1.00 (Table 1). The relative crystallinity generally increased with the calcination temperature and time, with the calcination temperature again having the most significant effect. The relative crystallinity increased steadily from 0.31 to 0.39 when the calcination temperature increased from 500 to 650 °C, then increased rapidly from 0.39 to 1.00 when the calcination temperature increased from 650 to 800 °C. Thus higher calcination temperatures led to materials with increased crystallinity, a positive factor for increasing the charge diffusion, thereby decreasing the recombination rate of the electron/hole pair. This is expected to positively influence the photocatalytic activity of the titania materials.

To investigate the interior structure of the mesoporous beads and crystal properties of titania, the samples were ultra-

Table 1. Crystal size, Crystallinity, and Porosity of the Mesoporous Anatase Beads after Calcination from 500 to 800 °C for 2 h, or Calcination at 650 °C from 2 to 24 h.

	calcined for 2 h at various temperatures (°C)							calcined at 650 °C for various times (h)			
temperature or time	500	550	600	650	700	750	800	4	8	12	24
crystal size (nm)[a]	12.7	13.7	14.2	17.5	23.2	50.5	55.0	17.9	21.6	22.9	25.8
relative crystallinity[b]	0.31	0.35	0.36	0.39	0.54	0.96	1.00	0.40	0.47	0.51	0.60
porosity (%)[c]	60	58	56	52	37	29	22	51	45	47	46

[a]Using the Scherrer equation at 2θ of 25.26°. [b]According to the average ratio of respective peak intensity of anatase peaks to that of the sample with the highest crystallinity (the beads calcined at 800 °C for 2 h). [c]On the basis of the density and pore volume from liquid N_2 gas sorption measurement, according to the equation of $P_m = V_p/(d^{-1} + V_p)$.[41]

microtomed to ~90 nm in thickness and analyzed using TEM, as shown in Figure 3. Each bead was composed of titania

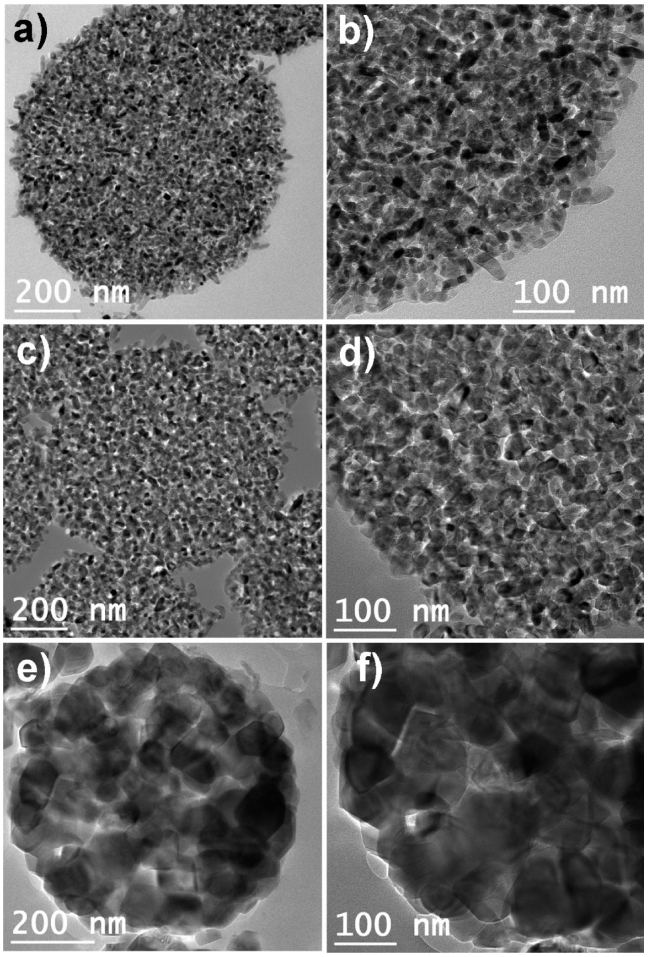

Figure 3. TEM images of the mesoporous TiO_2 beads calcined at (a, b) 500, (c, d) 650, and (e, f) 800 °C for 2 h.

nanoparticles that increased in size for higher calcination temperature, especially above 650 °C, confirming the X-ray powder diffraction results.

3.4. Surface and Optical Properties of the Beads. The mesopores from the voids between the anatase crystals were apparent (Figure 3). The Barrett–Joyner–Halenda (BJH) method was used to analyze the pore size distribution of the mesoporous beads using the adsorption branch of the gas sorption isotherm. The beads had a uniform pore size distribution centered in the mesopore range. Figure 4 shows the variation in pore size (solid curve) for the different calcination temperatures (Figure 4a) and times (Figure 4b).

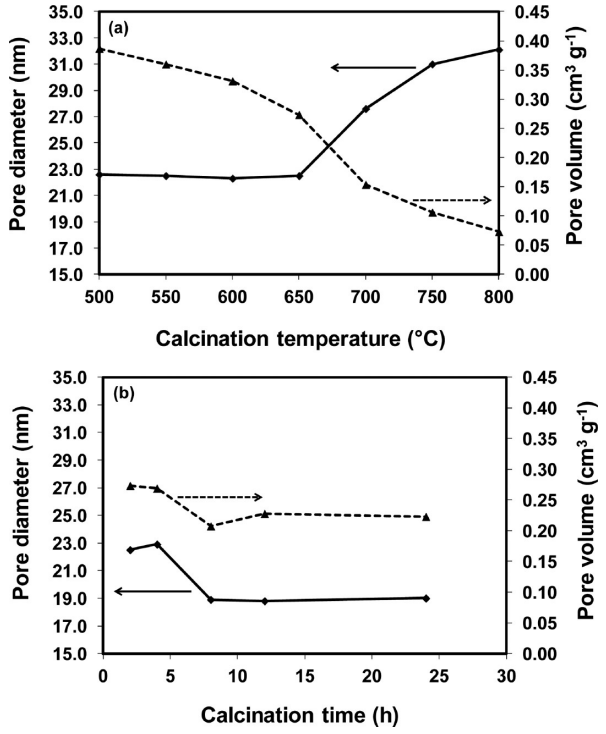

Figure 4. Pore size (diamonds) and pore volume (triangles) as a function of (a) calcination temperature from 500 to 800 °C for 2 h and (b) time from 2 to 24 h at 650 °C, calculated using the BJH model on the adsorption branch of the gas sorption isotherm.

For calcinaton temperatures below 650 °C, the pore diameter was constant at ~23 nm, and then it increased sharply to 32 nm as the calcination temperature increased to 800 °C. This change was a result of crystal growth as a function of calcination temperature. Calcination temperatures below 650 °C induced a gradual growth in crystal size that had minimal effect on the pore size, however above 650 °C, the significant crystal growth enlarged the interparticle voids. Contrarily, an increase in calcination time showed the opposite trend, the pore size decreased initially then remained constant even though the crystal size showed a gradual growth. This could result from more intimate packing of the crystals with prolonged calcination time. Pore volume (Figure 4 dashed line) showed an overall decrease as either calcination temperature or time increased. This was due to the overall shrinkage of materials resulting from the heat treatment and/or enlarged crystals occupying some pore space.

Photocatalytic reactions rely on surface chemistry.[6] An accessible high surface area is an important parameter for an efficient photocatalyst, as this should provide more active centers and allow organic pollutants to adsorb on the surface to

facilitate the first step of this reaction. The surface area of the mesoporous beads decreased with increasing calcination temperature or time, Figure 5. For 2 h calcination, the surface

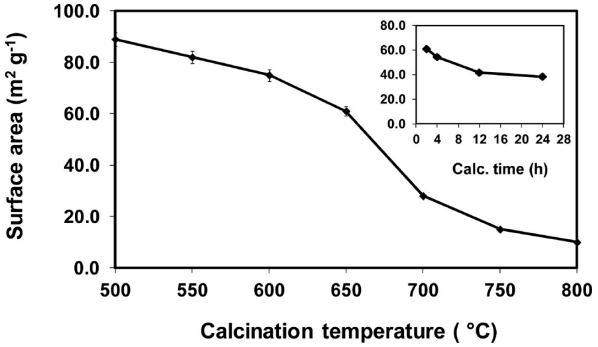

Figure 5. Surface areas of the mesoporous TiO_2 beads as a function of calcination temperature from 500 to 800 °C for 2 h, and (inset) the surface areas of the materials as a function of calcination time from 2 to 24 h at 650 °C.

area decreased gradually with increasing calcination temperature to 600 °C, then dropped significantly at 650 °C and higher. The inset shows the surface area decrease with calcination time for a calcination temperature of 650 °C. The decrease in surface area is related to the growth of the crystals within the beads (surface area is inversely proportional to the particle size). The porosity of the materials also plays an important role in the photocatalytic reaction. The high porosity allows more volume of the photocatalytic solution access to the active centers on internal surfaces of the TiO_2. The porosity of the beads, shown in Table 1, decreased gradually from 60% to 52% with increasing calcination temperature from 500 to 650 °C, and then dropped sharply to 22% with further increase in temperature to 800 °C. However, the porosity decreased slightly from 52% to 45% with increasing calcination time from 2 to 8 h, then remained relatively constant with further increase in calcination time. This would indicate again that longer calcination time benefited the packing of the crystals.

The number of surface hydroxyl groups is another important parameter for photocatalytic activity, as OH free radicals are formed and this is generally believed to promote the photocatalytic activity.[45] The peaks centered at around 3200 - 3500 and 1630 cm^{-1} in the FT-IR spectra are associated with the surface hydroxyl group and adsorbed water. These peaks decreased significantly for samples that underwent increased calcination temperature or time (see Figure 6), indicating removal of surface hydroxyl groups. Condensation reactions between surface hydroxyl groups (Ti-OH) occurred forming Ti-O-Ti for higher calcination temperatures and longer calcination durations. Increasing the calcination temperature from 500 to 700 °C, the peaks related to the surface hydroxyl groups decreased dramatically, and were no longer apparent (or were beyond the detection limit of the instrument) when further elevating the calcination temperature above 700 °C (Figure 6a). Compared with the calcination temperature correlation, the peak of the surface hydroxyl group drops steadily with increasing calcination time (Figure 6b).

The diffuse UV–vis reflectance spectra were measured to study the optical properties of the anatase beads, and showed strong absorption in UV light, Supporting Information Figure S1. The similarity in reflectance of mesoporous TiO_2 beads

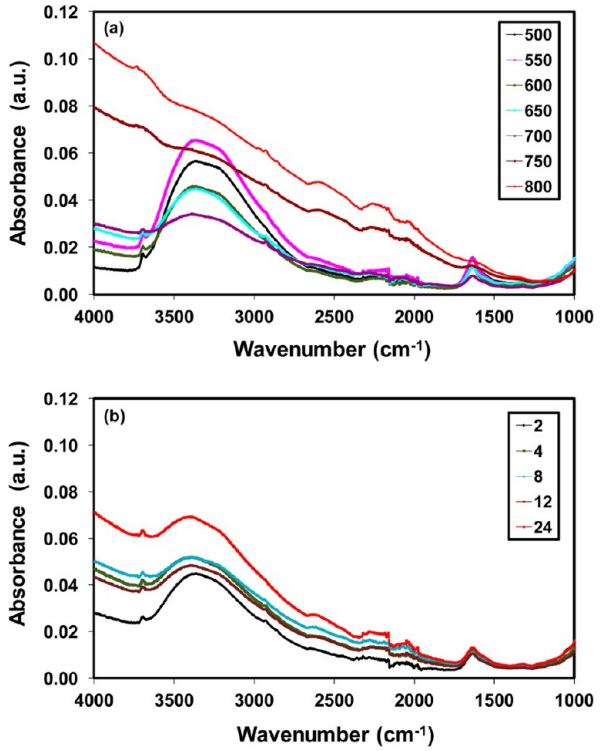

Figure 6. FTIR spectra of the mesoporous TiO_2 beads with various (a) calcination temperatures (°C) and (b) times (h).

regardless of the variation in calcination temperature or time, resulted in the same band gap for all samples (3.2 ± 0.1 eV).

3.5. Photocatalytic Activity of the Beads. The photocatalytic activity of the mesoporous TiO_2 beads was assessed by monitoring the photocatalytic degradation of methylene blue (MB), which is a typical effluent from the textile industry. The mesoporous TiO_2 beads were soaked in a 50 ppm MB aqueous solution in the dark with initial sonication for 20 min, then shaking overnight to achieve the adsorption–desorption equilibrium. UV light was shone on the solution that was continuously stirred and aerated. The MB concentration was monitored every 15 min. The degradation rate of MB followed the pseudo-first-order reaction mechanism: $\ln(C_0/C_t) = kt$, where C_0, C_t, k, and t refer to the concentration of MB at 0 min and t min, reaction rate constant, and photodegradation time, respectively.

The photocatalytic activity was significantly influenced by the calcination temperature compared with the change in activity seen with variation in calcination time, Figure 7. The reaction rate constant, k, gradually increased from 0.033 to 0.047 min^{-1} when the calcination temperature increased from 500 to 650 °C, then decreased significantly to 0.018 min^{-1} as the temperature increased to 800 °C (Figure 7a). The calcined materials demonstrated much higher activity compared with the uncalcined beads (k = 0.009 min^{-1}, Supporting Information Figure S3), which was attributed to the relatively lower crystallinity as revealed in the XRD patterns (Supporting Information Figure S2) and the presence of the structure directing agent inhibiting equivalent access of the dye to the TiO_2. The maximum photocatalytic rate constant obtained for the material calcined at 650 °C was close to that of Degussa P25 nanoparticles, a commercial benchmark photocatalyst (0.050 min^{-1}). It is worth noting that the mesoporous beads have the advantage of ease of separation using a simple

dx.doi.org/10.1021/am401867s | ACS Appl. Mater. Interfaces 2013, 5, 9421–9428

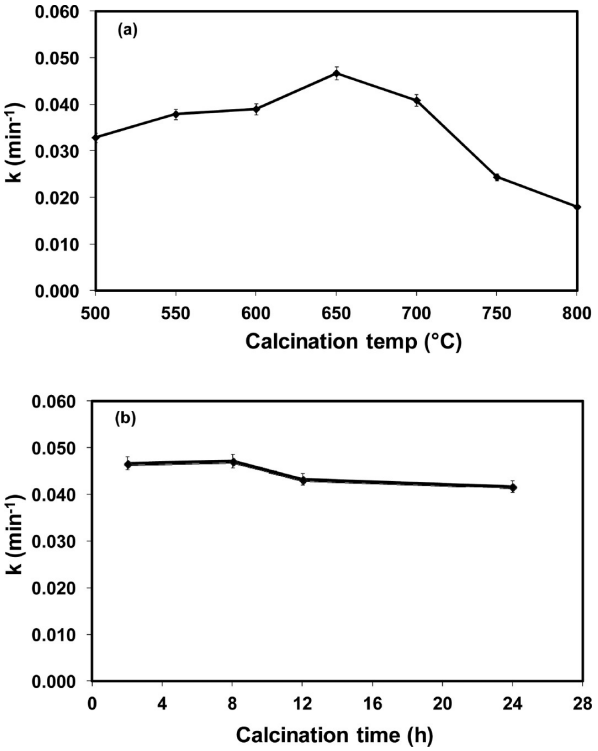

Figure 7. Photocatalytic rate constants of the mesoporous TiO_2 beads as a function of calcination (a) temperature for 2 h and (b) time at 650 °C.

sedimentation technique after the photocatalytic reaction, rather than the high speed centrifuge separation required for nanoparticulate Degussa P25, as the diameters of beads synthesized here (~700 nm) were 28 times larger than that of the Degussa P25 particles (~25 nm). As the sample calcined at 650 °C gave the highest photocatalytic rate constant, the effect of calcination time on the photocatalytic activity was studied for anatase beads calcined at 650 °C for a range of times from 2 to 24 h (Figure 7b). The photocatalytic activity of the beads did not vary when the calcination time increased from 2 to 8 h, whereas a marginal decrease in activity was observed when prolonging the calcination time to 12 and 24 h.

The photocatalytic activity is generally improved for samples with high crystallinity, large quantity of surface hydroxyl groups, high surface area, and high porosity. As discussed in this study, the crystallinity of the samples was inversely related to the surface hydroxyl group quantity and surface area: Increasing the calcination temperature or time, increased the crystal size and crystallinity of the anatase phase, however, decreased the amount of surface hydroxyl groups, surface area and the porosity. To visualize the synthesis-properties-photocatalytic activity relationship, the normalized material properties and photocatalytic rate constant have been superimposed for the varied calcination temperatures, Figure 8. The reaction rate constant was highest at a calcination temperature of 650 °C, because of increased crystallinity of the anatase phase, while rather high porosity and surface area were maintained. For temperatures above 650 °C, the reaction rate constant dropped significantly as a result of the decrease in surface area and porosity, even though the crystallinity of the sample increased further. The effect of crystallinity on the photocatalytic activity without variation in surface area cannot be determined, however the reaction rate constant per surface area has been

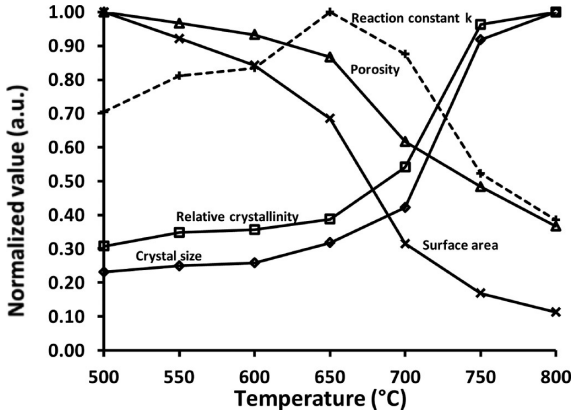

Figure 8. Calcination temperature effect on the materials properties and photocatalytic reaction rate constant, at normalized values.

plotted as a function of calcination temperature in Supporting Information Figure S4. This demonstrated an increase in the reaction rate constant per surface area with increasing calcination temperature because of the higher crystallinity of the anatase as a result of the higher temperature calcination. Anatase materials with higher crystallinity have less defects and grain boundaries, therefore more charge carriers (e.g., photon-excited electrons and holes) reach the surface of the crystal to initiate redox reactions. Both large quantities of charge carriers and surface hydroxyl groups will increase the apparent reaction rate constant.[46] At the higher calcination temperatures, especially above 700 °C, the number of surface hydroxyl groups were significantly decreased, hence the expected increase in the number of charge carriers from improved crystallinity could not compensate for this decrease. This indicates the importance of balancing these parameters during synthesis to achieve the optimum photocatalyst. The maximum photocatalytic activity was achieved for the material calcined at 650 °C, having a crystal size of 18 nm, surface area of 61 m^2 g^{-1}, and porosity of 52%. To demonstrate the importance of the bead porosity and structure, the mesoporous beads calcined at 650 °C for 8 h were crushed to powder with an agate mortar and pestle before conducting the photocatalytic reaction under the same conditions: The photocatalytic rate constant dropped 42% (k = 0.027 min^{-1}) compared with the initial intact beads (k = 0.047 min^{-1}). SEM (Supporting Information Figure S5) revealed that the spherical morphology was damaged after grinding, which confirmed that the structural properties of the spherical assemblies played an important role in enhancing the photocatalytic activity of the TiO_2 materials.

4. CONCLUSIONS

Mesoporous anatase titania beads with modified physical properties and varied photocatalytic activities were prepared by calcining the hybrid TiO_2 beads at different temperatures (from 500 to 800 °C) and times (from 2 to 24 h). The crystal size increased and the crystallinity of the anatase phase was enhanced with increasing calcination temperature and time. However, the surface area, surface hydroxyl group quantity, and bead diameter decreased with increasing calcination temperature and time. The pore size increased with calcination temperature but decreased with calcination time, due to the crystal growth for higher calcination temperature and more intimate packing of crystals with prolonged time. The changes in photocatalytic activity were primarily affected by the

calcination temperature; the maximum photocatalytic activity was achieved for the materials calcined at 650 °C for 2−8 h, which had a similar activity as the commercial Degussa P25 nanoparticles. The advantage of using the mesoporous anatase beads (~680−700 nm) was the ease of recovery after the photocatalytic reaction compared to recovery of Degussa P25 nanoparticles (~25 nm). The maximum photocatalytic activity results from a balance of high crystallinity, large number of surface hydroxyl groups, high surface area and high porosity. Overall, the calcination temperature had a more significant effect on the material properties and photocatalytic activity than calcination time. These findings will benefit the design of advanced and efficient TiO_2 based photocatalysts in the future.

■ ASSOCIATED CONTENT

Supporting Information

Diffuse reflectance UV−vis spectra of mesoporous TiO_2 beads, XRD patterns of the mesoporous TiO_2 beads after solvothermal treatment, photocatalytic degradation data for the uncalcined beads, SEM images of crushed TiO_2 beads, and photocatalytic reaction rate constant normalized for surface area. This information is available free of charge via the Internet at http://pubs.acs.org/.

■ AUTHOR INFORMATION

Corresponding Author

*E-mail: rcaruso@unimelb.edu.au. Fax: 61 3 9347 5180. Tel: 61 3 8344 7146.

Notes

The authors declare no competing financial interest.

■ ACKNOWLEDGMENTS

A portion of this research was undertaken on the powder diffraction beamline at the Australian Synchrotron, Victoria, Australia (P2318, P2671 and P3030); we especially acknowledge the beamline scientist Dr Qinfen Gu for assistance, and Dr Maryline Chee Kimling and Ms Sarah Harvey for participating in the sample measurements. Dr Simon Crawford is acknowledged for ultramicrotoming samples. The Advanced Microscopy Facility, Bio21 at The University of Melbourne is acknowledged for access to microscopes. This work was financially supported by the OCE Science Leader Scheme at CSIRO and the Australian Research Council through the Discovery Project scheme (DP110101346). RAC acknowledges the Australian Research Council for a Future Fellowship (FT0990583).

■ REFERENCES

(1) Kubacka, A.; Fernandez-Garcia, M.; Colon, G. *Chem. Rev.* **2012**, *112*, 1555−614.
(2) Tong, H.; Ouyang, S.; Bi, Y.; Umezawa, N.; Oshikiri, M.; Ye, J. *Adv. Mater.* **2012**, *24*, 229−251.
(3) Chen, X.; Mao, S. S. *Chem. Rev.* **2007**, *107*, 2891−2959.
(4) Fujishima, A.; Honda, K. *Nature* **1972**, *238*, 37−38.
(5) Hoffmann, M. R.; Martin, S. T.; Choi, W. Y.; Bahnemann, D. W. *Chem. Rev.* **1995**, *95*, 69−96.
(6) Linsebigler, A. L.; Lu, G. Q.; Yates, J. T. *Chem. Rev.* **1995**, *95*, 735−758.
(7) Hagfeldt, A.; Gratzel, M. *Chem. Rev.* **1995**, *95*, 49−68.
(8) Wang, X. D.; Caruso, R. A. *J. Mater. Chem.* **2011**, *21*, 20−28.
(9) Wang, X. D.; Mitchell, D. R. G.; Prince, K.; Atanacio, A. J.; Caruso, R. A. *Chem. Mater.* **2008**, *20*, 3917−3926.
(10) Wang, X.; Waterhouse, G. I. N.; Mitchell, D. R. G.; Prince, K.; Caruso, R. A. *ChemCatChem* **2011**, *3*, 1763−1771.
(11) Asahi, R.; Morikawa, T.; Ohwaki, T.; Aoki, K.; Taga, Y. *Science* **2001**, *293*, 269−271.
(12) Wang, X.; Blackford, M.; Prince, K.; Caruso, R. A. *ACS Appl. Mater. Interfaces* **2012**, *4*, 476−482.
(13) Ye, M.; Zhang, Q.; Hu, Y.; Ge, J.; Lu, Z.; He, L.; Chen, Z.; Yin, Y. *Chem. Eur. J.* **2010**, *16*, 6243−6250.
(14) Chen, F.; Xie, Y. D.; Zhao, J. C.; Lu, G. X. *Chemosphere* **2001**, *44*, 1159−1168.
(15) Aprile, C.; Corma, A.; Garcia, H. *Phys. Chem. Chem. Phys.* **2008**, *10*, 769−783.
(16) Testino, A.; Bellobono, I. R.; Buscaglia, V.; Canevali, C.; D'Arienzo, M.; Polizzi, S.; Scotti, R.; Morazzoni, F. *J. Am. Chem. Soc.* **2007**, *129*, 3564−3575.
(17) Sakatani, Y.; Grosso, D.; Nicole, L.; Boissiere, C.; Soler-Illia, G.; Sanchez, C. *J. Mater. Chem.* **2006**, *16*, 77−82.
(18) Li, Y.; Sasaki, T.; Shimizu, Y.; Koshizaki, N. *J. Am. Chem. Soc.* **2008**, *130*, 14755−14762.
(19) Fan, X.; Fei, H.; Demaree, D. H.; Brennan, D. P.; John, J. M. S.; Oliver, S. R. J. *Langmuir* **2009**, *25*, 5835−5839.
(20) Drisko, G. L.; Zelcer, A.; Wang, X.; Caruso, R. A.; Soler-Illia, G. J. d. A. A. *ACS Appl. Mater. Interfaces* **2012**, *4*, 4123−4130.
(21) Madhugiri, S.; Sun, B.; Smirniotis, P. G.; Ferraris, J. P.; Balkus, K. J. *Microporous Mesoporous Mater.* **2004**, *69*, 77−83.
(22) Wang, Y. W.; Zhang, L. Z.; Deng, K. J.; Chen, X. Y.; Zou, Z. G. *J. Phys. Chem. C* **2007**, *111*, 2709−2714.
(23) Liu, M.; Piao, L.; Lu, W.; Ju, S.; Zhao, L.; Zhou, C.; Li, H.; Wang, W. *Nanoscale* **2010**, *2*, 1115−1117.
(24) Fukahori, S.; Ichiura, H.; Kitaoka, T.; Tanaka, H. *Environ. Sci. Technol.* **2003**, *37*, 1048−1051.
(25) Xiang, Q.; Yu, J.; Jaroniec, M. *Chem. Commun.* **2011**, *47*, 4532−4534.
(26) Kim, D. S.; Kwak, S. Y. *Appl. Catal., A* **2007**, *323*, 110−118.
(27) Liu, Z. Y.; Sun, D. D.; Guo, P.; Leckie, J. O. *Chem. Eur. J.* **2007**, *13*, 1851−1855.
(28) Yu, J.; Zhang, J. *Dalton Trans.* **2010**, *39*, 5860−5867.
(29) Li, H.; Bian, Z.; Zhu, J.; Zhang, D.; Li, G.; Huo, Y.; Li, H.; Lu, Y. *J. Am. Chem. Soc.* **2007**, *129*, 8406−8407.
(30) Ming, H.; Ma, Z.; Huang, H.; Lian, S.; Li, H.; He, X.; Yu, H.; Pan, K.; Liu, Y.; Kang, Z. *Chem. Commun.* **2011**, *47*, 8025−8027.
(31) Araujo, P. Z.; Luca, V.; Bozzano, P. B.; Bianchi, H. L.; Soler-Illia, G. J. d. A. A.; Blesa, M. A. *ACS Appl. Mater. Interfaces* **2010**, *2*, 1663−1673.
(32) Tsung, C.-K.; Fan, J.; Zheng, N.; Shi, Q.; Forman, A. J.; Wang, J.; Stucky, G. D. *Angew. Chem., Int. Ed.* **2008**, *47*, 8682−8686.
(33) Chen, D.; Huang, F.; Cheng, Y.-B.; Caruso, R. A. *Adv. Mater.* **2009**, *21*, 2206−2210.
(34) Huang, F. Z.; Chen, D. H.; Zhang, X. L.; Caruso, R. A.; Cheng, Y. B. *Adv. Funct. Mater.* **2010**, *20*, 1301−1305.
(35) Sauvage, F.; Chen, D. H.; Comte, P.; Huang, F. Z.; Heiniger, L. P.; Cheng, Y. B.; Caruso, R. A.; Graetzel, M. *ACS Nano* **2010**, *4*, 4420−4425.
(36) Chen, D.; Cao, L.; Huang, F.; Imperia, P.; Cheng, Y.-B.; Caruso, R. A. *J. Am. Chem. Soc.* **2010**, *132*, 4438−4444.
(37) Chen, X.; Shen, S.; Guo, L.; Mao, S. S. *Chem. Rev.* **2010**, *110*, 6503−6570.
(38) Amano, F.; Yamakata, A.; Nogami, K.; Osawa, M.; Ohtani, B. *J. Am. Chem. Soc.* **2008**, *130*, 17650−17651.
(39) Yu, J. G.; Yu, H. G.; Cheng, B.; Zhao, X. J.; Yu, J. C.; Ho, W. K. *J. Phys. Chem. B* **2003**, *107*, 13871−13879.
(40) Nolan, N. T.; Seery, M. K.; Pillai, S. C. *J. Phys. Chem. C* **2009**, *113*, 16151−16157.
(41) Benkstein, K. D.; Kopidakis, N.; van de Lagemaat, J.; Frank, A. J. *J. Phys. Chem. B* **2003**, *107*, 7759−7767.
(42) Sclafani, A.; Herrmann, J. M. *J. Phys. Chem.* **1996**, *100*, 13655−13661.
(43) Benko, G.; Skarman, B.; Wallenberg, R.; Hagfeldt, A.; Sundstrom, V.; Yartsev, A. P. *J. Phys. Chem. B* **2003**, *107*, 1370−1375.
(44) Wang, X.; Dornom, T.; Blackford, M.; Caruso, R. A. *J. Mater. Chem.* **2012**, *22*, 11701−11710.

(45) Ding, Z.; Lu, G. Q.; Greenfield, P. F. *J. Phys. Chem. B* **2000**, *104*, 4815−4820.
(46) Carneiro, J. T.; Savenije, T. J.; Moulijn, J. A.; Mul, G. *J. Phys. Chem. C* **2010**, *114*, 327−332.